Remote sensing of sea surface wind speed under non-rainy conditions using X-band ground brightness temperatures at low elevation angles

Zhongqing Cao and Lixin Guo*
Xidian University, School of Physics and Optoelectronic Engineering, Xi'an, China

Abstract. Low elevation angles (between −3 deg and 3 deg) under bright temperatures (LEATBs) have not been efficiently employed in microwave remote sensing. LEATB data with horizontal polarization in the X-band and sea surface wind speed (SSWS) data, measured during an experiment in 2019, showed that when the SSWS is ≤ 4.9 m/s, the relationship between the brightness temperature ratio and SSWS is the opposite of that when the SSWS is over 4.9 m/s. Investigating the causes of this event, a LEATB-based simplified SSWS remote sensing method was developed. The results demonstrated that when the SSWS is below 4.9 m/s, the root mean squared error (RMSE) of the SSWS sensing is as low as 0.9544 m/s. However, when the SSWS exceeds 4.9 m/s, the corresponding RMSE is bound to 1.1349 m/s. [DOI: 10.1117/1.JRS.16.024508]

Keywords: low elevation angle brightness temperature; microwave radiometer; sea surface wind speed; X-band brightness temperature.

Paper 210617 received Sep. 22, 2021; accepted for publication Mar. 16, 2022; published online May 2, 2022.

1 Introduction

Microwave radiometers are frequently employed for passive remote sensing of the sea surface and atmospheric parameters. Measuring the brightness temperature (TB) of microwave radiation emitted by the sea surface or atmosphere and extracting standard oceanographic and meteorological parameters are the primary functions of microwave radiometers.[1,2] Numerous advancements have been made in the development of space-based microwave radiometers with varying frequencies and polarizations for monitoring sea surface and atmospheric profiles. The first-generation wind vector retrieval technique for the WindSat polarimetric radiometer was developed in 2006.[3] In the same year, marine surface winds observed with the Advanced Microwave Scanning Radiometer (AMSR) were compared to those measured by the off-shore moored buoy.[4] Wind speeds observed by AMSR were consistent with buoy observations, with a root mean squared error (RMSE) of 1.27 m/s for wind speeds beyond 5 m/s.

The satellite microwave radiometer, AMSR2, has been proposed to improve the spatial resolution of sea surface temperature (SST) reconstructions.[5] Numerous earlier studies have concentrated mainly on the sea surface at extreme wind speeds. Fore et al.[6] evaluated the sensitivity of the Soil Moisture Active Passive radiometer to ocean surface winds of up to 70 m/s. Along with high frequency (HF) and X-band radars,[7–9] sea surface parameters can also be measured using ground-based microwave radiometers. Zhang et al.[10] developed a ground-based microwave radiometer for monitoring sea surface wind speed (SSWS).

Continuous measurements of lower atmospheric temperatures and humidity are attainable using a ground-based microwave radiometer.[11,12] With the progress of tomography technologies, scanning microwave radiometers allowed for an increase in the spatial resolution of the inverse water vapor profile.[13–15] Tropospheric refraction and tropospheric duct can also be monitored using ground-based microwave scanning radiometers.[16,17] Compared to TBs applications with a wide elevation angle (>10 deg), low elevation angle brightness temperatures (LEATBs) have

---

*Address all correspondence to Lixin Guo, lxguo@xidian.edu.cn

been underutilized due to their complex generation mechanism and a dearth of data. Following the SSWS sensing basic theory introduced by Wentz,[18] the authors previously published some preliminary results of the effect of SSWS on LEATBs.[19] Nevertheless, no extensive analysis of the LEATBs from a radiometric perspective has been carried out. Due to the scarcity of measurements on the high seas, only a limited amount of information was released on LEATB about the state of the high seas (SSWS above 5 m/s).

This study makes use of LEATB data with horizontal polarization in the X-band, collected during September and October 2019 at the Bohe Marine Meteorological Science Experimental Base, Guangdong Province, China, under SSWS ranging from 0 to 10 m/s. It was found that when the SSWS falls below 4.9 m/s, the relationship between TB ratio and SSWS is opposite to that when the SSWS is above 4.9 m/s. This phenomenon was analyzed, and the feasibility of using LEATB in SSWS remote sensing was assessed according to the measured data.

The remainder of this study is organized as follows. The methodology is described in Sec. 2. The data and measurement details are presented in Sec. 3, and the results are reported in Sec. 4. The paper is then concluded in Sec. 5.

2 Methodology

For a shore-based scanning microwave radiometer, the primary TB component is the atmospheric downdraft TB when facing the sky. However, the main TB component is the sea surface upstream TB (SSUTB) when facing the sea surface. Wentz[18] derived SSUTB with polarization ε, $\mathrm{Tb}_{\mathrm{upwelling}}(\vec{k}_i,\varepsilon)|_0$, as

$$\begin{aligned}\mathrm{Tb}_{\mathrm{upwelling}}(\vec{k}_i,\varepsilon)|_0 &= E(\vec{k}_i,\varepsilon)T_s + [1-E(\vec{k}_i,\varepsilon)]\mathrm{Tb}_{\mathrm{downwelling}}(\vec{k}_r)|_0\\ &\quad + (4\pi\cos\theta_i)^{-1}\int_{2\pi} \mathrm{d}\vec{k}_s\cdot\Omega(\vec{k}_r,\vec{k}_s)[\sigma^0(\vec{k}_s,\varepsilon,\vec{k}_i,\varepsilon)+\sigma^0(\vec{k}_s,\varepsilon*,\vec{k}_i,\varepsilon)],\end{aligned} \tag{1}$$

where the first term on the right-hand side of the equation represents TB emission from the sea surface; the second term indicates the reflected atmospheric TB; and the integral I_Ω denotes the diffuse scattering component TB of atmospheric radiation. Furthermore, $E(\vec{k}_i,\varepsilon)$ is the emissivity of the sea surface in the direction $\vec{k}_i$, T_s is the SST in Kelvin, $\mathrm{Tb}_{\mathrm{downwelling}}(\vec{k}_r)|_0$ is the downdrafting TB at the sea surface (DTBSS) in the direction of $\vec{k}_r$ that is reflected off the sea surface, and $\Omega(\vec{k}_r,\vec{k}_s)$ is the fluctuation of the downdrafting TB relative to $\mathrm{Tb}_{\mathrm{downwelling}}(\vec{k}_r)|_0$. The term $\sigma^0(\vec{k}_s,\varepsilon,\vec{k}_i,\varepsilon)$ refers to the bistatic normalized radar cross-section (NRCS) for ε polarized radiation incident along $\vec{k}_s$ and ε polarized radiation scattered along $\vec{k}_i$. Another NRCS in Eq. (1) depends on scattered ε^* polarized radiation, where ε^* is the polarization state orthogonal to ε.

Wentz approximated the diffuse scattering integral, I_Ω, as given by[18]

$$I_\Omega = \omega_1 U_* \cdot \mathrm{Tb}_{\mathrm{downwelling}}(\vec{k}_r)|_0[1-E(\vec{k}_i,\varepsilon)], \tag{2}$$

where U_* is the friction velocity, and ω_1 denotes its coefficient. The friction velocity can be estimated using the SSWS average at a height of 6 m (U) above the sea surface (ASS)[20]

$$U_* = 0.033U. \tag{3}$$

A horizontally polarized SSUTB is deduced from Eqs. (1)–(3) as

$$\begin{aligned}\mathrm{Tb}_{\mathrm{upwelling}}(\theta_0,\varphi_0,\varepsilon_\parallel)|_0 &= E(\theta_0,\varphi_0,\varepsilon_\parallel)T_s + [1-E(\theta_0,\varphi_0,\varepsilon_\parallel)]\mathrm{Tb}_{\mathrm{downwelling}}(\vec{k}_r)|_0\\ &\quad + \omega U\cdot\mathrm{Tb}_{\mathrm{downwelling}}(\vec{k}_r)|_0[1-E(\theta_0,\varphi_0,\varepsilon_\parallel)],\end{aligned} \tag{4}$$

where θ_0, φ_0, and $\varepsilon_\parallel$ are elevation angle, azimuth angle, and horizontal polarization, respectively, and $\omega = 0.033\cdot\omega_1$. Equation (4) is applicable under conditions when the SSWS ranges from 6 to 21 m/s.[18]

The emissivity of the sea surface, $E(\theta_0, \varphi_0, \varepsilon_{\parallel})$ is given as

$$E = E_s + \Delta E. \tag{5}$$

The emissivity of a specular water surface at low elevation angles, E_s, is specified to be equal to or less than unity. The total variations in emissivity, ΔE, caused by roughness, wind direction, and foam, can be represented as[18]

$$\Delta E = m_1 U_* = mU, \tag{6}$$

where m and m_1 are two coefficients, with m being correlated with m_1 as $m = 0.033 \cdot m_1$.

The TB ratio, $\mathrm{Tb}_{\mathrm{upwelling}}(-\theta_0, \varphi_0, \varepsilon_{\parallel})|_0 / \mathrm{Tb}_{\mathrm{downwelling}}(\vec{k}_r)|_0$, is obtained from Eqs. (4)–and (6) and is given by

$$\frac{\mathrm{Tb}_{\mathrm{upwelling}}(-\theta_0, \varphi_0, \varepsilon_{\parallel})|_0}{\mathrm{Tb}_{\mathrm{downwelling}}(\vec{k}_r)|_0} = \frac{mU \cdot T_s}{\mathrm{Tb}_{\mathrm{downwelling}}(\vec{k}_r)|_0} + 1 - mU + \omega U - \omega m U^2. \tag{7}$$

Excluding small quantities of higher order, i.e., $-\omega m U^2$, from Eq. (7) yields

$$\frac{\mathrm{Tb}_{\mathrm{upwelling}}(-\theta_0, \varphi_0, \varepsilon_{\parallel})|_0}{\mathrm{Tb}_{\mathrm{downwelling}}(\vec{k}_r)|_0} = \left(\frac{T_s}{\mathrm{Tb}_{\mathrm{downwelling}}(\vec{k}_r)|_0} - 1\right) \cdot mU + 1 + \omega U. \tag{8}$$

3 Data

3.1 *2019 LEATB Measurement Campaign*

The China Research Institute of Radiowave Propagation (CRIRP) conducted a LEATB measurement experiment at the Bohe Marine Meteorological Science Experimental Base in Guangdong, China, from September to October 2019, to evaluate the potential application of LEATB in the range of −3 deg to 3 deg in remote sensing of wind speed over the sea. An X-band ground-based microwave radiometer and a marine meteorological observation platform were respectively deployed for measurements at sites A and B in Fig. 1. An X-band ground-based microwave radiometer was pointed towards the southwest open sea to gather TB scan angle data. The marine meteorological observation platform was an integrated observation platform. Throughout the experiment, meteorological data such as temperature, humidity, pressure, wind speed, and wind direction, were collected every ten seconds at various altitudes above the sea surface. In this study, the SSWS data were measured at 6 m ASS to develop a remote sensing model of the SSWS.

3.2 *Ground-Based Microwave Radiometer*

A dual-polarized, full-power, vertical and horizontal X-/Ku-band was utilized for the LEATB sensing. The microwave radiometer system was equipped with a ground-based microwave radiometer with a 1.8 m elliptic paraboloid antenna and an offset fed. Both the antenna feed and the receiver were installed in a thermostatic box to ensure thermal stability during operation. A wave-transparent mask made of polytetrafluoroethylene was installed between the feeder and the antenna surface. Table 1 lists the basic radiometer parameters. As indicated in Table 1, the microwave radiometer utilized in this study comprises various calibration loads to determine TBs based on the output voltage of the microwave radiometer receiver.[19]

The microwave radiometer was mounted on the ground at an elevation of 8 m above sea level during the experiment, as illustrated in the bottom-left of Fig. 1. The radiometer was pointed toward the open sea, and there were no islands within 300 km in the direction of observation (azimuth 135 deg).

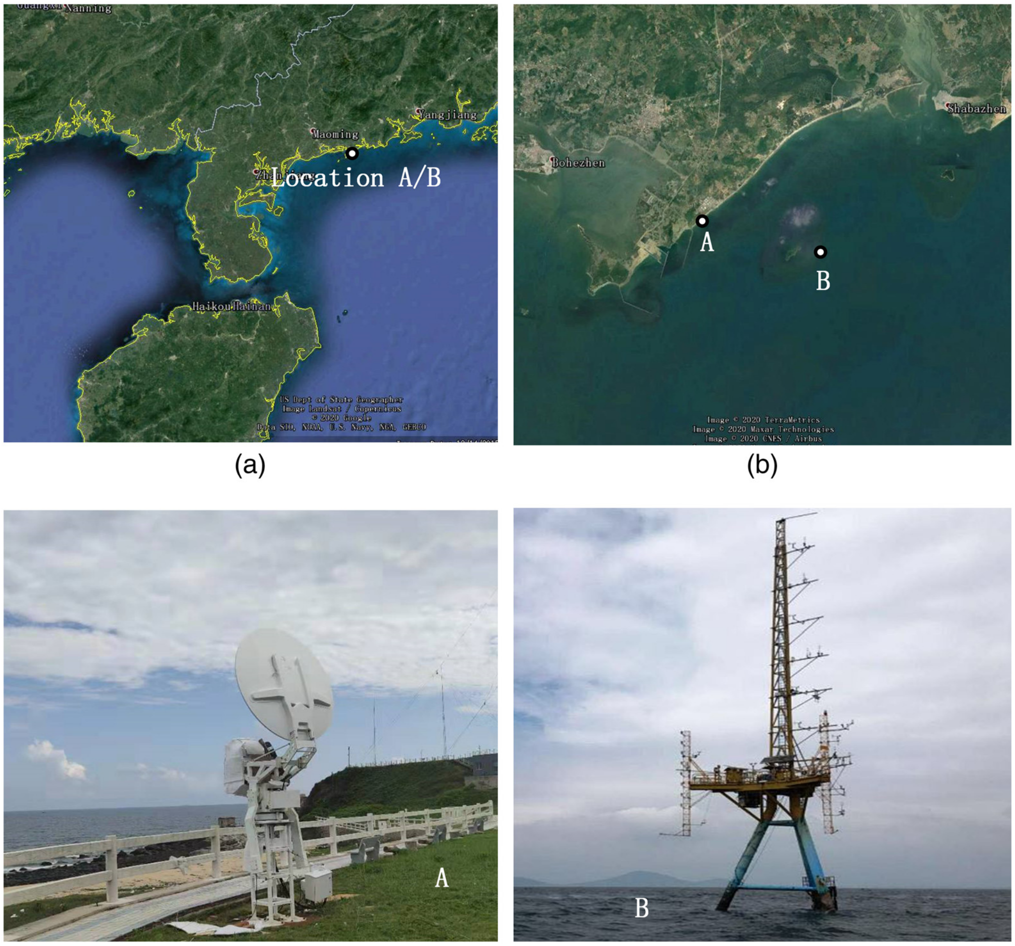

(a) (b)

(c) (d)

Fig. 1 Experimental sites and equipment. (a) A map of the experimental sites. (b) A magnified replica of the one to (a). (c) An X-band ground-based microwave radiometer located at point A. (d) The marine meteorological observation platform located at point B (~6 km offshore). Figures (a) and (b) were taken from Google Earth.

Table 1 Basic parameters of the measuring radiometer.

Parameter	Value
Center frequency	11 GHz
Bandwidth	300 MHz
Radiometer sensitivity	0.15 K (1 s integral time)
Preset elevation sequences (deg)	−4.5, −3.5, −2.7, −2.2, −1.9, −1.6, −1.3, −1.1, −0.9, −0.5, 0.1, 0.5, 0.7, 0.9, 1.2, 1.5, 1.8, 2.3, 3.1, 4.1
Sidelobe suppression	>40 dB
Elevation guidance resolution	0.01 deg
Feed box temperature stability	<0.05 K
Calibration techniques	Liquid nitrogen Noise diode Built-in ambient temperature black body

The radiometer measured the scanning elevation angle between −5 deg and 5 deg in accordance with a predetermined elevation sequence. Through the measurement, the antenna came to a halt at each elevation in the TB measurements sequence and then relocated to the next elevation until the completion of the entire sequence.

3.3 *Data Processing Method*

In the course of the experiment, sweep elevation angle was measured typically once per hour on days without rain, from 8:00 am to 6:00 pm, yielding a total of 65 scan angles. However, to exclude the influence of dense fog and thick clouds, DTBSS values over 140 K were eliminated at an elevation of 0.9 deg. Thus, a total of 53 full sweep angle measurements were taken on both sunny and cloudy days to develop the SSWS remote sensing model.

The microwave radiometer antenna utilized in this study has a 3 dB beamwidth of ~1.1 deg. When the radiometer is monitored at a very low elevation angle between −0.6 deg and 0.6 deg, within the antenna's beamwidth of 3 dB, both atmospheric DTBSSs at positive elevation angles and SSUTBs at negative elevation angles are present. To avoid remote sensing accuracy degradation due to TB mixed radiation, TB data measured at extremely low elevation angles, i.e., −0.5 deg, 0.1 deg, and 0.5 deg, are eliminated during data pre-processing. To specify the SSWS coefficients of remote sensing in Eq. (8), TB data with an elevation angle of < -0.6 deg and >0.6 deg are substituted for $\mathrm{Tb}_{\mathrm{upwelling}}(\theta_0, \varphi_0, \varepsilon_{\parallel})|_0$ and $\mathrm{Tb}_{\mathrm{downwelling}}(\vec{k}_r)|_0$, respectively. The elevation angle of the direction vector $\vec{k}_r$ is set at $-\theta_0$. After sampling the SSWS data at a height of 6 m above the sea surface, a 5-min average wind speed, U, is derived. Afterward, the 5-min average SSWS data corresponding to the scanned TBs is extracted and stored as a separate vector. Finally, the least-squares method is used to calibrate the coefficients in Eq. (8).

4 Results

4.1 *Critical SSWS*

Figure 2 depicts the fitted diagram to the measured TB ratio versus the SSWS ratio data, with solid curves representing different elevation angles. The corresponding elevation angles of $(\mathrm{Tb}_{\mathrm{upwelling}}(\theta_0, \varphi_0, \varepsilon_{\parallel})|_0$, $\mathrm{Tb}_{\mathrm{downwelling}}(\vec{k}_r)|_0)$ in Figs. 2(a)–2(d) are (−0.9 deg, 0.9 deg), (−1.1 deg, 1.2 deg), (−3.5 deg, 3.1 deg), and (−4.5 deg, 4.1 deg), respectively. Due to the absence of the DTBSS at 1.1 deg, 3.5 deg, and 4.5 deg elevations in Figs. 2(b)–2(d), DTBSS at 1.2 deg, 3.1 deg, and 4.1 deg elevations were employed instead, respectively, which introduces a margin of error. The dashed horizontal lines in Figs. 2(a) and 2(b) represent the critical SSWS, U_c, which lies between low and high SSWS, with a velocity of ~4.9 m/s. No value is reported for U_c in Figs. 2(c) and 2(d). At low wind speeds, i.e., $U < U_c$, the TB ratio increases with increasing SSWS, as illustrated in all Figs. 2(a)–2(d). However, at high wind speeds, i.e., $U > U_c$, distinct trends are found for different elevation angles of the DTBSS. In Figs. 2(a) and 2(b), the TB ratio decreases with increasing SSWS, but it remains stable in Fig. 2(c) and slightly increases in Fig. 2(d), as SSWS increases.

The phenomenon depicted in Fig. 2 can be explained in terms of the physical mechanism through which it was formed. As shown in Eq. (8), the TB ratio, $\mathrm{Tb}_{\mathrm{upwelling}}(-\theta_0, \varphi_0, \varepsilon_{\parallel})|_0/\mathrm{Tb}_{\mathrm{downwelling}}(\vec{k}_r)|_0$, is a function of the emissivity of the sea surface, E, (which is a function of SSWS and has a coefficient of m) and the sea surface scattering (which is a function of SSWS and has a coefficient of ω). Increases in SSWS[18] result in an increase in horizontally polarized sea surface emission, i.e., $m > 0$. As demonstrated in Eq. (4), the integral of the sea surface diffuse scattering, I_Ω, carries the influence of the wind speed-induced broadening of the scattering cone.[19] As illustrated in Fig. 3(a), the scattering direction of atmospheric radiation, $\vec{k}_i$, is solely defined by the direction of the atmospheric downwelling TB vector, $\vec{k}_r$, for the smooth sea surface and given by

$$\vec{k}_r = \vec{k}_i - 2(\vec{k}_i \cdot \vec{r})\vec{r}, \tag{9}$$

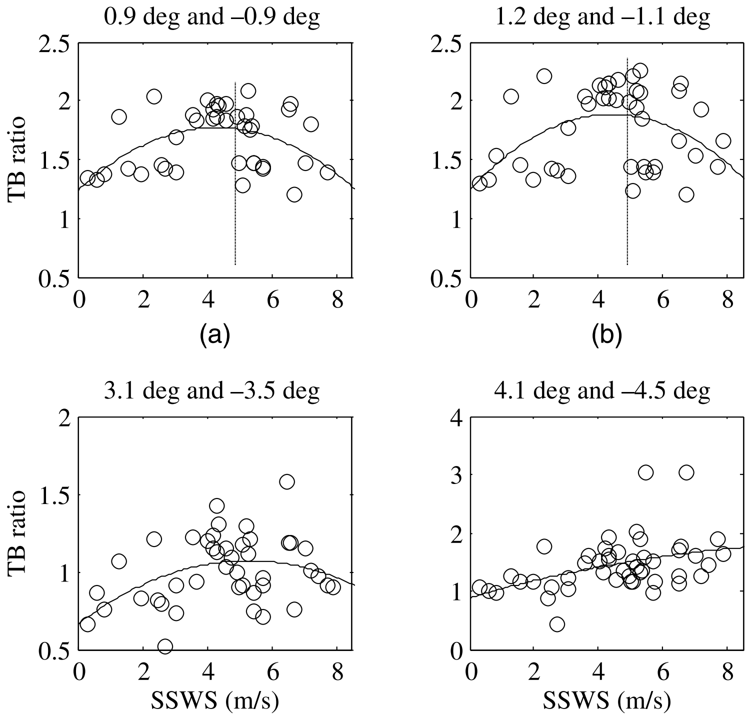

(a) (b)

(c) (d)

Fig. 2 The relationship between the TB ratio and the SSWS at various elevation angles. (a) 0.9 deg and -0.9 deg. (b) 1.2 deg and -1.1 deg. (c) 3.1 deg and -3.5 deg. (d) 4.1 deg and -4.5 deg. The circles in the figure represent the experimental data, whereas the solid lines represent the least squares fit results. The resulting regression formula reads as: $y = ax^2 + bx + c$, where y indicates the TB ratio and x denotes the SSWS. The dashed lines in Figs. 2(a) and 2(b) represent SSWS at the maximum TB ratio of the fitting curve, namely the critical SSWS, U_c.

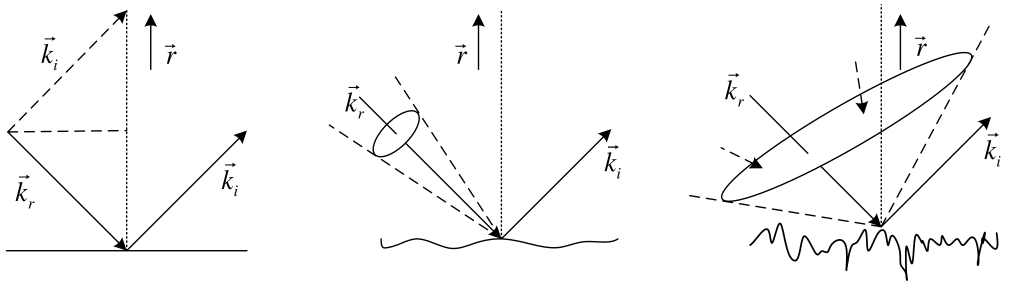

(a) Specular reflection

(b) Sea surface scattering at low wind speed

(c) Sea surface scattering at high wind speed

Fig. 3 The effect of wind speed on the broadening of the scattering cone. (a) Specular reflection. (b) Sea surface scattering at low wind speed. (c) Sea surface scattering at high wind speed.

where $\vec{r}$ is the earth radius vector normalized to unit length. At low wind speeds and rough sea surfaces, atmospheric downwelling radiation scatters in various directions. Additionally, as demonstrated in Fig. 3(b), the scattering power in the direction $\vec{k}_i$ is mainly determined by the incident power in the conical region with the central axis, $\vec{k}_r$. At high wind speeds and rough sea surfaces, however, the scattering cone widens, as illustrated in Fig. 3(c).

As illustrated in Fig. 4, when the elevation angle is 0.9 deg, the TB is about 75 K. At this point, given the sharp reduction in DTBSS with an increase in elevation angle, the beam broadening results in a considerable decrease in the weighted downwelling TB [weighted by the bistatic NRCS in the scattering cone, as shown in Figs. 3(b) and 3(c)]. DTBSS is around 30 K

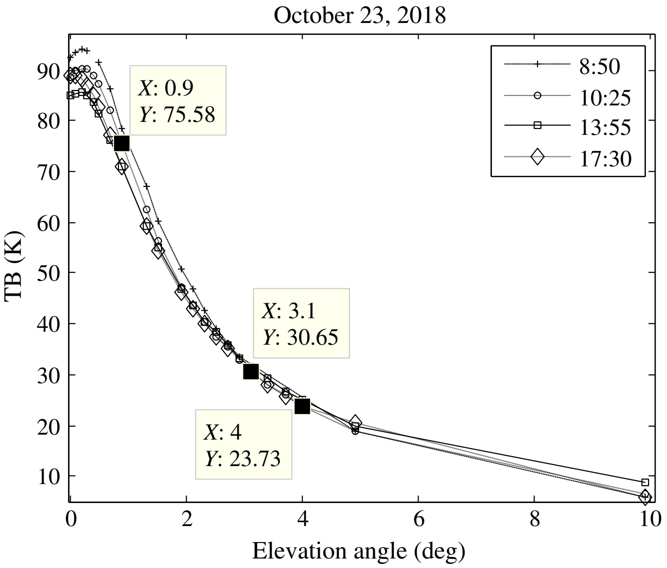

Fig. 4 X-band DTBSS versus elevation angle. The four curves in the figure were measured on October 23, 2018 at 8:50, 10:25, 13:55, and 17:30 local time, respectively (adopted from Ref. 19).

when the elevation angle is 3.1 deg. Additionally, the rate at which DTBSS decreases slows as the elevation angle increases. As a result, the effect of the weighted downwelling TB reduction caused by beam broadening grows slower. When the elevation angle is 4 deg, the TB is about 23 K, and the decreasing rate of DTBSS diminishes with the increase of elevation angle, as shown in Fig. 4. At this moment, the reduction effect of the weighted downwelling TB caused by scattering beam broadening is not readily apparent.

As seen in Figs. 2(a)–2(d), when $U < U_c$, the TB ratio increases with SSWS. This is due to the fact that at low wind speeds, the scattering of the sea surface varies slightly with the wind speed. Sea surface-emission varies significantly with wind speed and plays a dominant role in the relationship between TB ratio and SSWS, resulting in a rise in the TB ratio as SSWS increases. Ignoring the scattering integral in Eq. (8) results in

$$\frac{\mathrm{Tb}_{\text{upwelling}}(\theta_0,\varphi_0,\varepsilon_{\|})|_0}{\mathrm{Tb}_{\text{downwelling}}(\vec{k}_r)|_0}=\left(\frac{T_s}{\mathrm{Tb}_{\text{downwelling}}(\vec{k}_r)|_0}-1\right)mU+1. \tag{10}$$

Ignoring the change in the sea surface temperature, T_s, and DTBSS, $\mathrm{Tb}_{\text{downwelling}}(\vec{k}_r)|_0$, Eq. (10) is used to develop an expression of U for a low SSWS, which is given by

$$U=A\left[\frac{\mathrm{Tb}_{\text{upwelling}}(\theta_0,\varphi_0,\varepsilon_{\|})|_0}{\mathrm{Tb}_{\text{downwelling}}(\vec{k}_r)|_0}-1\right], \tag{11}$$

where $A=1/\{[T_s/\mathrm{Tb}_{\text{downwelling}}(\vec{k}_r)|_0-1]\cdot m\}$.

When $U > U_c$, the TB ratios of various elevation angles exhibit distinct variation trends with increasing SSWS, as illustrated in Figs. 2(a)–2(d). As the SSWS increases, the scattering cone expands, resulting in a drop in the DTBSS weight in the specular direction, $\vec{k}_r$, and an increase in the DTBSS weight at high elevation angles (>5 deg) in the diffuse scattering integral, I_Ω. In the low elevation range between 0 deg and 3 deg, the X-band DTBSS is significantly higher than that at high elevation angles. Furthermore, as seen in Fig. 4, it drops rapidly as the elevation angle increases.[19] Therefore, as illustrated in Figs. 2(a) and 2(b) for low elevation angles between 0.9 deg and 1.1 deg, considering an increase in SSWS, the effect of broadening the scattering cone leads to a faster drop in the diffuse scattering integral, I_Ω. It plays an important role in the relationship between the TB ratio and SSWS, leading to a decrease in the TB ratio at high wind speeds. As indicated in Figs. 2(c) and 4, when the elevation angle exceeds 3 deg, for example, 3.5 deg, the DTBSS declining trend with elevation angle gradually slows down.[19] The broadening of the scattering cone results in a more gradual decrease in the scattering integral, I_Ω, as SSWS increases. With increased SWSS, the rise in TB ratio is roughly encountered by the increase in sea surface radiation, leaving the TB ratio remains almost unchanged. Furthermore, at a higher elevation angle, such as 4.5 deg in Fig. 2(d), the DTBSS itself is relatively small, and the downward trend with increasing elevation angle is less noticeable, as illustrated in Fig. 4. The declining trend in the scattering integral, induced by the broadening of the scattering cone, becomes less apparent as SSWS increases. Additionally, the radiative effect of the sea surface contributes significantly to the interaction between TB and SSWS.[19] Since the sea surface radiation increases with rising SSWS,[18] the TB ratio increases as well, as indicated in Fig. 2(d).

Due to the existence of critical SSWS, U_c, a TB ratio corresponding to two SSWS, one within the interval $U < U_c$ and another within the interval $U > U_c$, cannot determine whether the SSWS is within the interval $U < U_c$ or $U > U_c$ only using TB ratios of elevation angle combinations in Figs. 2(a) and 2(b). It can be seen from Fig. 2(d) that the TB ratio of the elevation angle combination of 4.1 deg and −4.5 deg rises as the wind speed increases. Since each TB ratio corresponds to a unique SSWS, the wind speed interval in which the SSWS is located may be predicted using this elevation angle combination.

At low elevation angles, when $U > U_c$, disregarding the change in sea surface emission, E, in Eq. (4) and setting E to a constant value of E_0, yields

$$\frac{\mathrm{Tb}_{\text{upwelling}}(\theta_0,\varphi_0,\varepsilon_\parallel)|_0}{\mathrm{Tb}_{\text{downwelling}}(\vec{k}_r)|_0}=\frac{E_0T_s}{\mathrm{Tb}_{\text{downwelling}}(\vec{k}_r)|_0}+(1-E_0)+(1-E_0)\omega U. \tag{12}$$

Ignoring variations in sea surface temperature, T_s, and DTBSS, $\mathrm{Tb}_{\text{downwelling}}(\vec{k}_r)|_0$, the expression of U for a high SSWS can be obtained as

$$U=B\frac{\mathrm{Tb}_{\text{upwelling}}(\theta_0,\varphi_0,\varepsilon_\parallel)|_0}{\mathrm{Tb}_{\text{downwelling}}(\vec{k}_r)|_0}+C, \tag{13}$$

where $B=1/[\omega(1-E_0)]$, $C=-E_0T_s/[\omega(1-E_0)\mathrm{Tb}_{\text{downwelling}}(\vec{k}_r)|_0]-1/\omega$.

4.2 *Analysis*

In Figs. 5(a)–5(i), $\mathrm{Tb}_{\text{upwelling}}(\theta_0,\varphi_0,\varepsilon_\parallel)|_0$ and $\mathrm{Tb}_{\text{downwelling}}(\vec{k}_r)|_0$ are determined to be (0.7 deg, −0.9 deg), (0.7 deg, −1.1 deg), (0.7 deg, −1.3 deg), (0.9 deg, −0.9 deg), (0.9 deg, −1.1 deg), (0.9 deg, −1.3 deg), (1.2 deg, −1.1 deg), (1.2 deg, −1.3 deg), and (1.2 deg, −1.6 deg), respectively. Table 2 reports the corresponding coefficients A–C in Eqs. (11) and (13) as well as their respective RMSEs (RMSE1 corresponds to Eq. (11), and RMSE2 corresponds to Eq. (13)). For example, the second row of Table 2 contains the coefficients of the SSWS remote sensing model based on the elevation angle combination of 0.7 deg and −0.9° deg and the corresponding RMSEs. The first column reports the elevation combination, and the second column reports the fitting value of A in Eq. (11) using this elevation combination, where Eq. (11) is the remote sensing model in the SSWS interval $U < U_c$. The third column represents the RMSE of the model defined in Eq. (11). The fourth and fifth columns provide the fitting values of B and C in Eq. (13), respectively, where Eq. (13) is the remote sensing model in the SSWS interval $U > U_c$. The sixth column reports the RMSE of the model defined in Eq. (13). As shown in Fig. 5, it can be found in combinations of angles of (0.7 deg, −0.9 deg), (0.9 deg, −0.9 deg), and (1.2 deg, −1.1 deg) that the TB ratio increases with increasing SSWS at low wind speed ($U < U_c$), while it decreases with increasing SSWS at high wind speed ($U > U_c$). This finding indicates that these angle combinations satisfy the relationships between the low-elevation angle (−3 deg, 3 deg) TB ratio and SSWS described in Sec. 4.1. Furthermore, the relationship between SSWS and TB ratio is shown to vary with elevation angle. The explanation for this could be that sea surface factors such as waves, foam, and wave shielding effects all have a significant effect on electromagnetic waves at various elevation angles.[18] This results in distinct patterns of variations in the reflectivity of the sea surface and scattering from SSWS at different elevation angles. Moreover, the DTBSSs differ depending on the elevation angles at which they

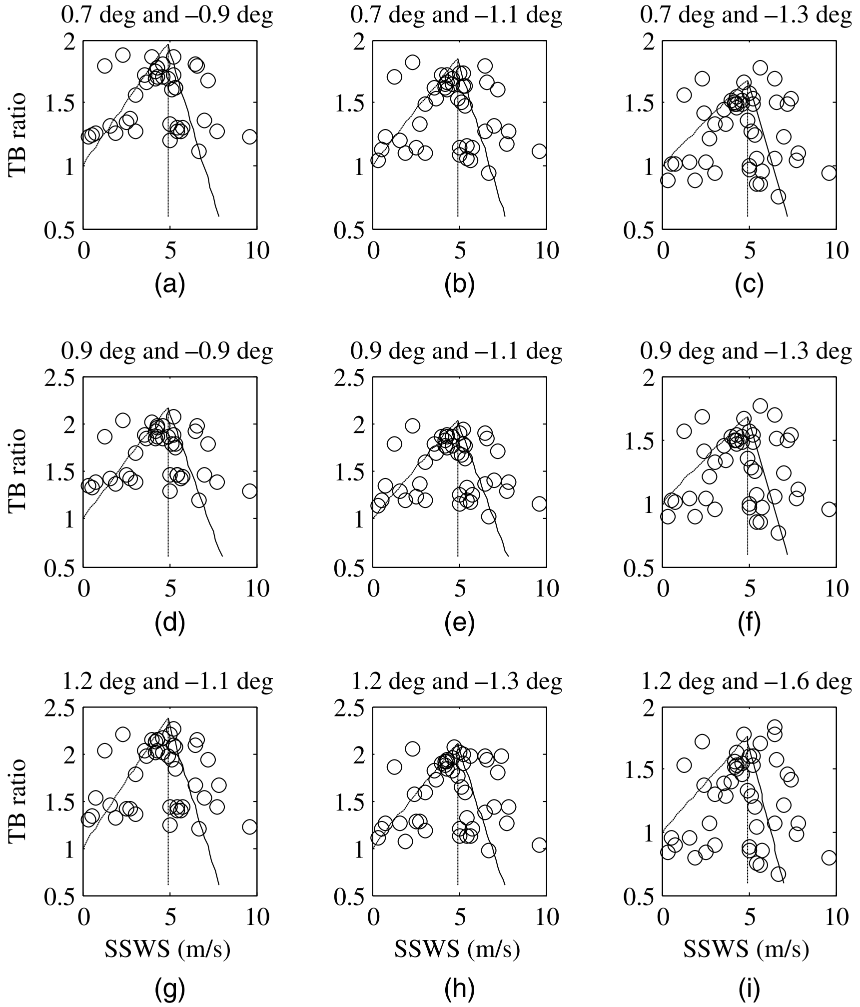

Fig. 5 The relationship between SSWS and TB ratio. (a) 0.7 deg and -0.9 deg, (b) 0.7 deg and -1.1 deg, (c) 0.7 deg and -1.3 deg, (d) 0.9 deg and -0.9 deg, (e) 0.9 deg and -1.1 deg, (f) 0.9 deg and -1.3 deg, (g) 1.2 deg and -1.1 deg, (h) 1.2 deg and -1.3 deg, and (i) 1.2 deg and -1.6 deg. The circles represent data measured from September through October, 2019. The dashed vertical line represents SSWS $= Uc$. The dashed line in the figure represents a least squares fit to Eq. (11) based on the measurement data at $U < Uc$. The solid oblique line in the figure is fitted using the least square method in accordance with Eq. (13) based on the measurement data when $U > Uc$. The slope of the dashed line TB ratio at SSWS $= Uc$ is adjusted to be the same as the slope of the solid line when SSWS $= Uc$.

are measured. As indicated in Table 2, the maximum modeling accuracies in terms of RMSEs are obtained when the upward and downward elevations of TBs are 0.9 deg and -0.9 deg, respectively. Comparing Figs. 5(d)–5(f) reveal that RMSE1 and RMSE2 are 0.9544 and 1.1349 m/s, respectively, when the combination of elevation angles is 0.9 deg and -0.9 deg. Additionally, when the combination is 0.9 deg and -1.1 deg, the RMSE1 and RMSE2 are calculated as 1.0704 and 1.1901 m/s, respectively. For the combination of 0.9 deg and -1.3 deg, RMSE1 and RMSE2 are determined as 1.2639 and 1.2477 m/s, respectively. It can be seen that the RMSE of the fitting is at its minimum when the elevation angle of $\mathrm{Tb}_{\mathrm{upwelling}}(\theta_0, \varphi_0, \varepsilon_{\parallel})|_0$ is mirrored by the elevation of $\mathrm{Tb}_{\mathrm{downwelling}}(\vec{k}_r)|_0$. Additionally, the RMSE increases as the DTBSS and SSUTB elevation angles deviate from the mirror image. Upon further comparison of Figs. 5(a)–5(c), or Figs. 5(g)–5(i), it can be found that this rule still holds. This indicates that in a real remote sensing measurement if the elevation measurements taken by the radiometer are not accurate enough, the remote sensing error will increase.

Table 2 Fitting coefficients for various combinations of elevations.

Elevation angle (deg)	A	RMSE1 (m/s)	B	C	RMSE2 (m/s)
0.7 and 0.9	5.0522	1.0279	−2.3411	9.5117	1.1771
0.7 and −1.1	5.7668	1.2144	−2.1932	8.9568	1.2281
0.7 and −1.3	7.0013	1.5518	−2.0375	8.3635	1.2729
0.9 and −0.9	4.1663	0.9544	−2.136	9.5481	1.1349
0.9 and −1.1	4.7453	1.0704	−2.043	9.0526	1.1901
0.9 and −1.3	5.9655	1.2639	−2.013	8.5665	1.2477
1.2 and −1.1	3.5679	1.0142	−1.6937	8.9196	1.1631
1.2 and −1.3	4.4439	1.0914	−1.7118	8.4994	1.2516
1.2 and −1.6	6.109	1.9018	−1.6334	7.8435	1.2685

Due to the lack of synchronous radar-measured wind field data during the 2019 LEATB measurement campaign, this research compares the accuracy of SSWS remote sensing to the accuracy of radar-measured wind fields in previous literature. In this context, Xie et al.[8] compared the wind field data measured by shipborne high-frequency surface wave radar to buoys data and found that the RMSE of radar measurements of wind speed was limited to 1.43 m/s. Huang et al.[9] evaluated the data of sea surface wind speed obtained from X-band nautical radar images using anemometer measurements as a reference and concluded that the RMSE of the measured wind speed value was 1.31 m/s. It can be seen from Table 2 that the accuracy of SSWS obtained using the remote sensing method presented in this study is slightly higher than that achieved by HF and X-band radar.

Because the radiometer is a passive microwave radiation receiver, it benefits from low power consumption. But, the radiometer's remote sensing result of SSWS is the average SSWS at its observation direction. By adjusting the azimuth angle of the radiometer, the microwave radiometer can monitor the SSWS at various azimuth angles. However, microwave radiometers, unlike radars, cannot monitor the two-dimensional wind field with varying ranges and azimuth angles.

In this section, the TB ratios of the low elevation angle combinations are solely employed to establish remote sensing models in two SSWS intervals, i.e., $U < U_c$ and $U > U_c$, respectively. In this paradigm, one TB ratio corresponds to two SSWS values. In practical remote sensing applications, the TB ratio of the elevation angle combination of 4.1 deg and −4.5 deg can be used to determine the interval of SSWS, i.e., $U < U_c$ or $U > U_c$. Then, the TB ratio of the low elevation angle combinations, e.g., (0.7 deg, −0.7 deg), (0.9, −0.9 deg), (1.1 deg, −1.1 deg), and (1.5 deg, −1.5 deg), can be used to reverse more precise SSWS values within this interval. The SSWS interval can be determined with greater precision by considering additional potentially suitable combinations of higher elevations. For instance, it should be determined whether the relationship between the TB ratio of elevation angle combinations, such as (6 deg, −6 deg) and (7 deg, −7 deg), and wind speed is monotonous. Due to the scarcity of TB ratio data for the high-elevation angle combination (elevation of downwelling TB should be >3 deg and elevation of upwelling TB should be <-3 deg) obtained during the 2019 LEATB measurement campaign, this paper proposes only a method to determine the interval of SSWS in practice.

5 Conclusion

Due to the complicated mechanism by which LEATBs are formed and their intrinsic scarcity, they have been exploited inefficiently. In this study, SSWS sensing has been investigated from a microwave perspective. To this end, numerous selected samples of horizontally polarized X-band LEATBs were employed at various elevation angles. Furthermore, a remote sensing formulation was developed between SSWS and LEATBs at low and high wind speeds, and the coefficients were calibrated using the measured data. At low wind speeds, the RMSE of remote sensing SSWS is found to be 0.9544 m/s. In contrast, at higher wind speeds, the RMSE of remote sensing SSWS is 1.1349 m/s. Nonetheless, additional experiments will be required to acquire a deeper understanding of the SSWS sensing mechanism and its nature. Additional data on high seas and rainy days will be required in the future to investigate the determination of wind speed under such conditions. Additionally, the influence of wind direction deserves further investigation. In addition, when only low elevation, i.e., between −3 deg and 3 deg, TBs are employed for SSWS remote sensing, one TB ratio may correspond to two SSWS values. By adding combinations of elevations, e.g., −4.5 deg and 4.1 deg, a unique wind speed can be obtained at the sea surface. The next step is to determine the unique SSWS by comparing the TB ratios of multiple elevation angle combinations.

Due to the dual-polarization nature of the microwave radiometer employed in this paper, wind direction remote sensing is accompanied by a fuzzy problem.[21,22] In addition, the data obtained to model wind direction was insufficient. Therefore, only SSWS was monitored using X-band horizontal polarization TB in this paper. The next step is to monitor the wind direction and speed of the sea surface simultaneously using the full polarization microwave radiometer.

Acknowledgments

The authors appreciate Xianhai Cheng for his invaluable advice on the construction of the microwave radiometer. This study was supported by the National Natural Science Foundation of China (Grant Nos. 61627901, 61431010, and 61971385), as well as the Foundation for Innovative Research Groups of the National Natural Science Foundation of China (Grant No. 61621005). The authors would like to express their gratitude to EditSprings for providing expert linguistic services.

References

1. S. Mack et al., “Extracting tidal variability of sea ice concentration from AMSR-E passive microwave single-swath data: a case study of the Ross sea,” *Geophys. Res. Lett.* **40**, 547–552 (2013).
2. T. Meissner et al., “The emissivity of the ocean surface between 6 and 90 GHz over a large range of wind speeds and earth incidence angles,” *IEEE Trans. Geosci. Remote Sens.* **50**, 3004–3026 (2012).
3. S. T. Brown et al., “An emissivity-based wind vector retrieval algorithm for the WindSat polarimetric radiometer,” *IEEE Trans. Geosci. Remote Sens.* **44**, 611–621 (2006).
4. N. Ebuchi, “Evaluation of marine surface wind speed observations from AMSR2 on GCOM-W satellite,” *IEEE J. Sel. Top. Appl. Earth Obs. Remote Sens.* **10**, 3955–3962 (2017).
5. T. Maeda et al., “Sea-surface-temperature retrieval at higher spatial resolution in the satellite-borne microwave radiometer AMSR2 follow-on mission,” *IEEE Geosci. Remote Sens. Lett.* **18**, 336–340 (2020).
6. A. G. Fore et al., “SMAP radiometer-only tropical cyclone intensity and size validation,” *IEEE Geosci. Remote Sens. Lett.* **15** (10), 1480–1484 (2018).
7. Z. Z. Chen et al., “Observation and intercomparison of wave motion and wave measurement using shore-based coherent microwave radar and HF radar,” *IEEE Trans. Geosci. Remote Sens.* **57**, 7594–7605 (2019).
8. J. H. Xie et al., “Measuring ocean surface wind field using shipborne high-frequency surface wave radar,” *IEEE Trans. Geosci. Remote Sens.* **56**, 3383–3397 (2018).
9. W. M. Huang et al., “An empirical mode decomposition method for sea surface wind measurements from X-band nautical radar data,” *IEEE Trans. Geosci. Remote Sens.* **55**, 6218–6227 (2017).
10. Y. Zhang et al., “Design and development of a ground-based microwave radiometer system,” in *Proc. Prog. Electromagn. Res. Symp. (PIERS ONLINE)*, Vol. 6, pp. 66–70 (2010).

11. R. Renju et al., "Atmospheric boundary layer characterization using multiyear ground-based microwave radiometric observations over a tropical coastal station," *IEEE Trans. Geosci. Remote Sens.* **55**, 6877–6882 (2017).
12. D. Liu et al., "Retrieval analysis of atmospheric water vapor for K-band ground-based hyperspectral microwave radiometer," *IEEE Geosci. Remote Sens. Lett.* **11**, 1835–1839 (2014).
13. S. Padmanabhan et al., "Retrieval of atmospheric water vapor density with fine spatial resolution using three-dimensional tomographic inversion of microwave brightness temperatures measured by a network of scanning compact radiometers," *IEEE Trans. Geosci. Remote Sens.* **47**, 3708–3721 (2009).
14. S. Steinke et al., "Water vapor tomography with two microwave radiometers," *IEEE Geosci. Remote Sens. Lett.* **11**, 419–423 (2014).
15. J. H. Schween et al., "Horizontal humidity gradient from one single scanning microwave radiometer," *IEEE Geosci. Remote Sens. Lett.* **8**, 336–340 (2011).
16. R. Sumati, "Statistical retrieval of the water vapor profiles using zenith-pointing and off-axis 22GHz radiometer measurements," PhD Thesis, The Pennsylvania State University, State College, University Park, Pennsylvania (1998).
17. V. Louf et al., "The seasonal and diurnal cycles of refractivity and anomalous propagation in the Sahelian area from microwave radiometric profiling," *J. Atmos. Ocean. Technol.* **33**, 2095–2112 (2016).
18. F. J. Wentz, "A model function for ocean microwave brightness temperatures," *J. Geophys. Res.* **88**(C3), 892–908 (1983).
19. Z. Q. Cao et al., "Characteristics and applications of the ground-based X band low elevation angle brightness temperatures under low sea state based on measured data," *Remote Sens.* **12**(11), 1736–1759 (2020).
20. S. SethuRaman and G. S. Raynor, "Surface drag coefficient dependence on the aerodynamic roughness of the sea," *J. Geophys. Res.* **80**, 4983–4988 (1975).
21. S. H. Yueh et al., "Polarimetric thermal emission from periodic water surfaces," *Radio Sci.* **29**(1), 87–96 (2016).
22. F. J. Wentz, "Measurement of oceanic wind vector using satellite microwave radiometers," *IEEE Trans. Geosci. Remote Sens.* **30**(5), 960–972 (1992).

Zhongqing Cao received his BE degree in electrical engineering from Herbin Institute of Technology, China, in 2009, and his MS degree in radiophysics from CRIRP, China, in 2012. He is currently pursuing a PhD in radiophysics at Xidian University.

Lixin Guo: is currently a professor and the head of the School of Physics and Optoelectronic Engineering, Xidian University. He has authored or coauthored 4 books and over 300 journal articles. His current research interests include electromagnetic wave propagation and scattering in complex and random media, computational electromagnetics, inverse scattering, and antenna analysis and design.